

LETTER TO THE EDITOR

The distribution of water in the high-mass star-forming region NGC 6334 I [★]

M. Emprechtinger^{1,20}, D. C. Lis¹, T. Bell¹, T. G. Phillips¹, P. Schilke^{10,20}, C. Comito¹⁰, R. Rolfs¹⁰, F. van der Tak¹⁶, C. Ceccarelli³, H. Aarts¹⁶, A. Bacmann^{3,2}, A. Baudry², M. Benedettini⁴, E.A. Bergin²⁵, G. Blake¹, A. Boogert⁵, S. Bottinelli⁶, S. Cabrit⁸, P. Caselli⁷, A. Castets³, E. Caux⁶, J. Cernicharo⁹, C. Codella¹¹, A. Coutens⁶, N. Crimier^{3,9}, K. Demyk⁶, C. Dominik^{12,13}, P. Encrenaz⁸, E. Falgarone⁸, A. Fuente¹⁴, M. Gerin⁸, P. Goldsmith¹⁵, F. Helmich¹⁶, P. Hennebelle⁸, T. Henning²⁶, E. Herbst¹⁷, P. Hily-Blant³, T. Jacq², C. Kahane³, M. Kama¹², A. Klotz⁶, J. Kooi¹, W. Langer¹⁵, B. Lefloch³, A. Loose²⁷, S. Lord⁵, A. Lorenzani¹¹, S. Maret³, G. Melnick¹⁸, D. Neufeld¹⁹, B. Nisini²⁴, V. Ossenkopf²⁰, S. Pacheco³, L. Pagani⁸, B. Parise¹⁰, J. Pearson¹⁵, C. Risacher¹⁶, M. Salez⁸, P. Saraceno⁴, K. Schuster²¹, J. Stutzki²⁰, X. Tielens²², M. van der Wiel¹⁶, C. Vastel⁶, S. Viti²³, V. Wakelam², A. Walters⁶, F. Wyrowski¹⁰, and H. Yorke¹⁵

(Affiliations can be found after the references)

Received May 31, 2010; accepted July 23, 2010

ABSTRACT

Aims. We present observations of twelve rotational transitions of H_2^{16}O , H_2^{18}O , and H_2^{17}O toward the massive star-forming region NGC 6334 I, carried out with *Herschel/HIFI* as part of the guaranteed time key program *Chemical HERschel Surveys of Star forming regions (CHESS)*. We analyze these observations to obtain insights into physical processes in this region.

Methods. We identify three main gas components (hot core, cold foreground, and outflow) in NGC 6334 I and derive the physical conditions in these components.

Results. The hot core, identified by the emission in highly excited lines, shows a high excitation temperature of ~ 200 K, whereas water in the foreground component is predominantly in the ortho- and para- ground states. The abundance of water varies between $4 \cdot 10^{-5}$ (outflow) and 10^{-8} (cold foreground gas). This variation is most likely due to the freeze-out of water molecules onto dust grains. The $\text{H}_2^{18}\text{O}/\text{H}_2^{17}\text{O}$ abundance ratio is 3.2, which is consistent with the $^{18}\text{O}/^{17}\text{O}$ ratio determined from CO isotopologues. The ortho/para ratio in water appears to be relatively low (1.6 ± 1) in the cold, quiescent gas, but close to the equilibrium value of three in the warmer outflow material (2.5 ± 0.8).

Key words. ISM: molecules — stars: formation

1. Introduction

Water is one of the most important coolants in star-forming regions, and is thus a key molecule in the process of star formation. Water plays a crucial role in the energy balance in protostellar objects, and therefore its abundance is an important parameter, especially in massive star-formation, because it influences the collapse and fragmentation of cloud cores. Furthermore H_2O (either in the gas phase or as ice on dust grains) is thought to contain a significant fraction of oxygen. Thus well constrained water abundances provide key input for astrochemical models of star-forming regions.

Most rotational lines of H_2O , including the ground-state transition of ortho- and para- H_2O , are not observable from the ground. However, previous space missions have already provided a glimpse of the water universe (ISO, van Dishoeck & Helmich 1996; SWAS, Melnick & Bergin 2005; Odin, Bjerkeli et al. 2009). The derived water abundance varies widely, between $\sim 10^{-4}$ in warm (> 100 K) gas and $\sim 10^{-8}$ in cold regions (e.g., Boonman et al. 2003). These differences in the H_2O abundance

are caused by the freeze-out of water molecules onto dust grains. Unfortunately, all the observations to date suffer from a shortage of accessible water lines (SWAS and Odin observed the ortho ground-state transition only, while ISO only detected excited lines) and low spatial resolution ($> 1'$).

Van der Tak et al. (2010) observed the para ground-state transition ($1_{11} - 0_{00}$) of H_2^{16}O in the high-mass protostellar object DR 21(Main) with the *Herschel* Space Observatory (Pilbratt et al. 2010). They found water abundances between 10^{-10} and 10^{-7} , about a factor 1000 lower than those derived in previous studies. This shows that the H_2O abundance in star-forming regions is not well understood and that studies including multiple lines of both ortho- and para- H_2O are highly desirable to put better constraints on the water abundance in the ISM. These capabilities are provided by the HIFI instrument (de Graauw et al. 2010).

In this letter, we present high spectral resolution observations of twelve H_2^{16}O , H_2^{17}O , and H_2^{18}O lines in the high-mass star-forming region NGC 6334 I. The relatively nearby (1.7 kpc; Neckel 1978) massive star-forming region NGC 6334 harbors sites of various stages of protostellar evolution (Straw & Hyland 1989). Single-dish continuum observations at sub-millimeter wavelength revealed a total mass of $16700 M_{\odot}$ (Matthews et al. 2008), of which $200 M_{\odot}$ is associated with NGC 6334 I (Sandell 2000). NGC 6334 I, studied exten-

[★] *Herschel* is an ESA space observatory with science instruments provided by European-led principal Investigator consortia and with important participation from NASA

sively over the last decades (e.g., Beuther et al. 2007, 2008; Hunter et al. 2006), is a molecular hot core associated with a cometary-shaped ultra compact H II (UCHII) region (de Pree et al. 1995), which exhibits a spectrum with very many emission lines (Schilke et al. 2006; Thorwirth et al. 2003). Furthermore, a bipolar outflow (Leurini et al. 2006; Beuther et al. 2008) and several masers have been detected (e.g., Kreamer & Jackson 1995; Ellingsen et al. 1996, Walsh et al 2007). Observations using the SMA showed that the hot core of NGC 6334 I itself consists of four compact condensations located within a $\approx 10''$ diameter region, which are emitting about 50% of the continuum detected in single-dish observations (Hunter et al. 2006).

2. Observations

We observed twelve water lines with frequencies between 488 GHz and 1.113 THz, which are listed in Table 2. These observations were conducted between March 1 and March 23, 2010, using *Herschel*/HIFI in the dual beam switch (DBS) mode as part of the guaranteed time key program *Chemical Herschel Spectral Surveys* (CHESS). The coordinates of the observed position in NGC 6334 I are $\alpha_{2000} : 17^h 20^m 53.32^s$ and $\delta_{2000} : -35^\circ 46' 58.5''$. We used the Wide Band Spectrometer (WBS) with a resolution of 1.1 MHz across a 4 GHz IF bandwidth. The spectra shown here are equally weighted averages of the H and V polarization, reduced with the HIPE pipeline (Ott 2010), version 2.6. We exported the resulting Level 2 double side band (DSB) spectra to the FITS format for a subsequent data reduction and analysis with the IRAM GILDAS package.

The spectral scans of NGC 6334 I consist of DSB spectra with a redundancy of eight, i.e., the lower and upper side band are observed with eight different local oscillator settings. This observing mode allows the deconvolution and isolation of the single sideband (SSB) spectra (Comito & Schilke 2002), which we present here.

The HIFI beam size at the frequencies observed is given in Table 2. For the main beam efficiency we assumed a value of 68%. The velocity calibration in HIFI data processed with HIPE 2.6 is subject to uncertainties of up to $\sim 2 \text{ km s}^{-1}$ due to an approximate model for the spacecraft velocity used. A comparison with a more accurate spacecraft velocity model indicates that the velocity scale for the data presented here has an uncertainty of $\leq 0.3 \text{ km s}^{-1}$.

3. Results and discussion

The spectra of the twelve observed water lines are displayed in Fig. 1. The shapes of these lines are in general very complex, indicating the complex structure of the source itself. They can be divided into three main components: the hot core, the cold foreground component, and the outflow. Although the spectrum of NGC 6334 I is in general very rich in emission lines, the water spectra presented here are relatively clean. Emission lines of other molecules interfering with the H₂O lines are only seen near H₂¹⁸O 2₁₁ – 2₀₂ (H₃C-O-CH₃) and H₂¹⁸O 1₁₀ – 1₀₁ (HNC and H₃COH).

Below we discuss the three individual components present in the water spectra.

3.1. Cold foreground gas

The foreground material as seen in the ground-state ortho- and para-H₂¹⁶O transitions, consists of three velocity components at

-6.3 ± 0.3 , -0.3 ± 0.12 , and $+6.2 \pm 0.15 \text{ km s}^{-1}$. All three components appear in absorption against the strong continuum emitted by the warm dust in the hot core of NGC 6334 I. The parameters of the absorption features seen in the 1₁₁-0₀₀ and the 1₁₁-1₀₁ spectra are listed in Table 3. The velocity of the different components are derived from Gaussian fits. However, Gaussian fits do not correctly match the depth of the absorption. Therefore the other parameters are determined by visually inspecting the spectra and integrating over the relevant velocity ranges. To derive the continuum level we applied a linear baseline fit in the vicinity of the absorption line. Thus the background radiation contains not only the dust continuum, but also water emission from all the components in the background (hot core and outflow). The velocity-averaged optical depths of the individual components derived from the line/continuum ratio of the 1₁₁ – 0₀₀ line (ground-state para transition) are 2.1 ± 0.83 , 1.27 ± 0.29 and 1.39 ± 0.63 for the -6.3 km s^{-1} , -0.3 km s^{-1} , and the $+6.2 \text{ km s}^{-1}$ component, respectively. The corresponding optical depths of the ground-state ortho transition are 1.79 ± 0.53 , 0.94 ± 0.20 , and 1.18 ± 0.38 . The velocity ranges over which the optical depths were averaged are given in Table 1. Deriving the optical depth from the line-to-continuum ratio is based on the assumption that the excitation temperature is negligible with respect to the continuum brightness temperature, i.e., that the foreground component is cold with respect to the background. The large uncertainties arise because the optical depth of deep absorption lines is very sensitive to the actual continuum level, which is determined with an accuracy of $\sim 5\%$ in our HIFI spectra. In addition, the frequency of the H₂O 1₁₁-1₀₁ (557 GHz) is close to the edges of the bands 1a and 1b. Thus the uncertainty is enhanced by variations in the sideband ratio of the receiver. For the present calculation we used a sideband imbalance of 5%, derived from the differences of the spectra taken in bands 1a and 1b. The lack of absorption of H₂¹⁸O 1₁₁ – 0₀₀ and H₂¹⁸O 1₀₁ – 1₁₀ at $+6.2 \text{ km s}^{-1}$ gives 1σ upper limits for the optical depth of the para- and ortho-H₂O ground-state transitions of 4.5 and 6.2, respectively, assuming an H₂¹⁶O/H₂¹⁸O ratio of 500, which constrains the optical depth at the line center even more.

Because almost the complete continuum signal is absorbed at -6.3 and 6.2 km s^{-1} , the absorbing material must be cold. Upper limits for the excitation temperature are 5.5 K and 9 K for the o-H₂O and p-H₂O, respectively. These upper limits are derived assuming large optical depths, thus the remaining signal at the center of the water lines corresponds to the source function of the transition, and therefore reflects the water excitation temperature.

In the following analysis we assume that all water molecules are in the ortho- and para-ground states. This assumption is justified given the very high critical densities of these two transitions ($2 \cdot 10^8 \text{ cm}^{-3}$ and $1.5 \cdot 10^7 \text{ cm}^{-3}$ for the ground-state para- and ortho-transitions, respectively). The column densities per velocity interval are thus given by the formula

$$N = \frac{8\pi \cdot \tau \cdot \nu^3}{c^3 A} \frac{g_l}{g_u},$$

where N is the column density, τ the optical depth, ν the line frequency, and c is the speed of light. A stands for the Einstein A coefficient and g_l and g_u are the degeneracy of the lower and the upper level of the transition. Subsequently, we integrated over the velocity ranges given in Table 1 to determine the column density for each component. For the -6.3 km s^{-1} component we considered only velocities $> -6 \text{ km s}^{-1}$, because at velocities $< -6 \text{ km s}^{-1}$ the signal may be contaminated by absorption in the

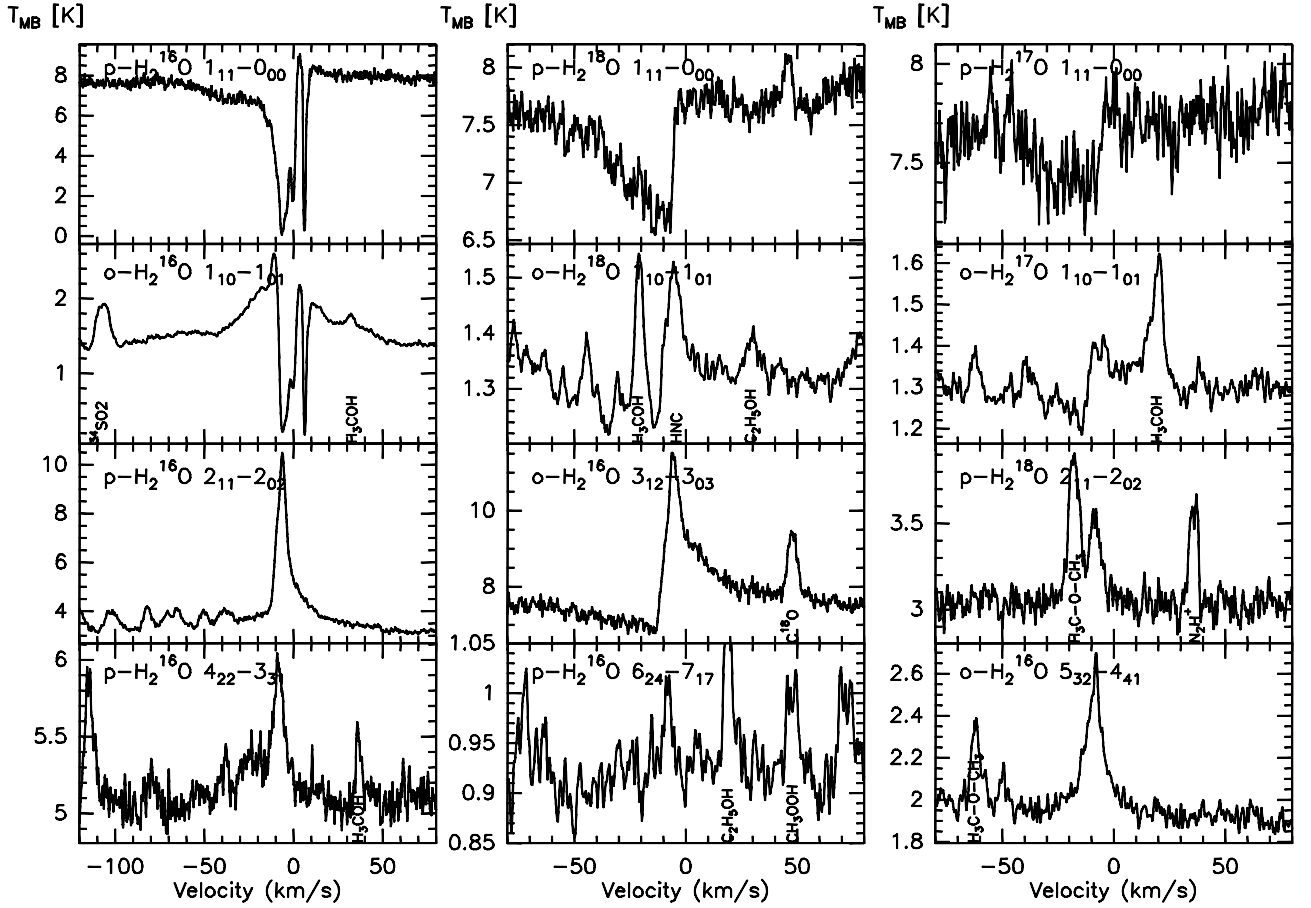


Fig. 1. Spectra of twelve water lines in the high-mass star-forming region NGC 6334 I. *Top row:* Ground-state para transitions of H_2^{16}O , H_2^{18}O and H_2^{17}O . *Second row:* Ground-state ortho transitions of H_2^{16}O , H_2^{18}O and H_2^{17}O . *Third row:* Water transitions with moderate upper state energies. *Bottom row:* Water lines with high upper state energies (> 400 K).

outflow. The derived column densities and the ortho/para (o/p) ratio of the three components are listed in Table 1. Because the uncertainties of the column densities are dominated by systematic errors (mainly by the uncertainty of the continuum level and baseline standing waves), the errors given in Table 1 are maximum uncertainties. The o/p ratio seems to be lower than three,

Table 1. Column densities of ortho and para water in the foreground material.

Comp.	vel. range kms^{-1}	$N(\text{o-H}_2\text{O})$ $10^{12} [\text{cm}^{-2}]$	$N(\text{p-H}_2\text{O})$ $10^{12} [\text{cm}^{-2}]$	o/p ratio
-6.3	-6 to -2	31.4 ± 9.4	19.3 ± 7.8	1.6 ± 0.8
-0.3	-2 to 1	14.2 ± 3.1	8.8 ± 2.0	1.6 ± 0.5
+6.2	5 to 8	17.8 ± 5.8	9.6 ± 4.3	1.8 ± 1.0

the value expected in statistical equilibrium, in all three foreground components. However, the uncertainties of the derived ratios are quite large for these highly saturated lines, and thus the derived o/p ratios have to be treated with caution.

Water is expected to be formed with an o/p ratio of three. Subsequently, collisions with atomic and molecular ions (e.g., H^+ , H_3^+) can lead to proton exchanges, and thus thermalization of the o/p ratio. In cool, dense gas, like the foreground components, an o/p ratio lower than three is thus likely. From the o/p ratio of 1.6 ± 0.5 derived for the -0.3 km s^{-1} component, which has the smallest uncertainty, we calculate a spin temperature of $19 \pm 5 \text{ K}$,

indicating that the temperature of the foreground component is $\sim 20 \text{ K}$. An o/p ratio lower than three has also been measured toward Sgr B2(M) (Lis et al. 2010; see this paper for further discussion).

3.2. Hot core

Spectra of $\text{H}_2^{16}\text{O} 4_{22} - 3_{31}$, $\text{H}_2^{16}\text{O} 6_{24} - 7_{17}$, and $\text{H}_2^{16}\text{O} 5_{32} - 4_{41}$, the three transitions with upper state energies above 400 K, show only a single component at a velocity of about -8.2 km s^{-1} , emitted by the hot core of NGC 6334 I. The parameters of these lines are listed in Table 4. Integrated intensities are derived by integrating over a velocity range, whereas the other parameters are derived by a Gaussian fit. This velocity is about 1.5 km s^{-1} lower than the systematic velocity of NGC 6334 I, but is consistent with the velocity seen in $\text{CH } J = \frac{3}{2} - \frac{1}{2}$ (van der Wiel et al. 2010) and $\text{HCO}^+ J = 12 - 11$. Interferometric observations of $\text{NH}_3 (3,3)$ and $(6,6)$ reveal a velocity of -8.1 km s^{-1} for one of the embedded cores (mm 2), which shows the highest optical depth in highly excited ammonia lines (Beuther et al. 2007). In addition to the high-energy H_2^{16}O lines the $\text{H}_2^{18}\text{O} 2_{11} - 2_{02}$ line ($E_{\text{up}} = 136.4 \text{ K}$) peaks at -8.6 km s^{-1} (Table 4), suggesting that this optically thin line is predominantly emitted from the hot core as well.

Two of the observed lines, $\text{H}_2\text{O} 5_{32} - 4_{41}$ and $\text{H}_2\text{O} 4_{22} - 3_{31}$ are expected to show maser activity over a wide range of physical conditions (Maercker et al. 2008; Neufeld & Melnick 1991),

therefore we excluded these lines from the subsequent analysis. To calculate the excitation temperature and water abundance in the hot core, we assumed that the two remaining lines are optically thin and that the levels are populated according to the Boltzmann distribution. Furthermore, we adopted an o/p ratio of three, an $\text{H}_2^{16}\text{O}/\text{H}_2^{18}\text{O}$ of 500, and, based on interferometric observations (Hunter et al. 2006) a source size of $\sim 10''$ to correct for the difference in the beam size. With these assumptions, we derive a water excitation temperature (T_{ex}) of 217 ± 30 K, and a total H_2^{16}O column density of $7.5 \pm 1.0 \cdot 10^{15} \text{ cm}^{-2}$.

The $\text{C}^{18}\text{O } J = 10 - 9$ line is observed very close to the $\text{o-H}_2^{16}\text{O } 3_{12} - 3_{03}$ line ($\Delta\nu = -202$ MHz) and allows us to independently estimate the H_2 column density of the hot core. The integrated intensity of this C^{18}O line is 8.78 K km s^{-1} , which results, assuming a similar excitation temperatures for C^{18}O and H_2O and local thermal equilibrium, in a C^{18}O column density of $7.2 \pm 1 \cdot 10^{14} \text{ cm}^{-2}$. This gives $N(\text{H}_2) = 3.8 \pm 0.5 \cdot 10^{21} \text{ cm}^{-2}$, adopting a CO abundance of $9.5 \cdot 10^{-5}$ and a $\text{C}^{16}\text{O}/\text{C}^{18}\text{O}$ ratio of 500, leading to a water abundance of $2.0 \pm 0.3 \cdot 10^{-6}$. The assumption of a similar excitation temperature of H_2O and C^{18}O is questionable considering the large difference in their dipole moments (C^{18}O is likely tracing a slightly more extended, cooler region). Sandell (2000) derives a dust temperature of 100 K for NGC 6334 I. Assuming 100 K as lower limit for T_{ex} of C^{18}O leads to a C^{18}O column density of $1.6 \cdot 10^{15} \text{ cm}^{-2}$, and subsequently to a lower limit of $8 \cdot 10^{-7}$ for the water abundance.

3.3. Outflow

Outflow features are seen in the ground-state ortho- and para-transitions of all three water isotopologues, except the $\text{H}_2^{18}\text{O } 1_{10} - 1_{01}$ line, which is contaminated by H_3COH and HNC lines. Furthermore, the outflow can be seen in the $\text{H}_2^{16}\text{O } 2_{11} - 2_{02}$ and $\text{H}_2^{16}\text{O } 3_{12} - 3_{03}$ lines (P-Cygni profiles). The spectrum of $\text{H}_2^{16}\text{O } 1_{10} - 1_{01}$ is very interesting because it shows indication of two outflow components, a broad pedestal ranging from -90 to $+60 \text{ km s}^{-1}$ and a narrower, but brighter component from -40 to $+20 \text{ km s}^{-1}$ (see Fig. 2). Because only one outflow is seen in interferometric observations (Beuther et al. 2008) and the central velocities of the two components are similar, the observed spectra likely reflect a temperature or density variation within the outflow.

That the blue outflow lobe shows up in emission in $\text{H}_2^{16}\text{O } 1_{10} - 1_{01}$, but weakly in absorption in $\text{H}_2^{17}\text{O } 1_{10} - 1_{01}$ may be explained by a higher excitation temperature of the optically thick H_2^{16}O line, caused by photon trapping, which in turn leads to level thermalization.

A prominent feature is the absorption against the hot core dust continuum in the blue lobe of the outflow seen in all ground-state transitions except $\text{H}_2^{16}\text{O } 1_{10} - 1_{01}$ (see Fig. 3). Because absorption features show up even in H_2^{17}O , which is ≈ 1500 times less abundant than H_2^{16}O , the H_2^{16}O lines are likely completely optically thick. Thus the signal in the $\text{H}_2^{16}\text{O } 1_{11} - 0_{00}$ line at velocities from -40 km s^{-1} to -20 km s^{-1} (6.82 ± 0.12 K) is the source function times the beam filling factor ($S \cdot \eta_B$) plus the dust continuum (7.72 K; see Fig. 2) not affected by absorption. At velocities higher than -20 km s^{-1} possible absorption by the foreground component makes the results unreliable, and therefore this velocity range was excluded from our analysis. From the emission in the red lobe seen in the $\text{H}_2^{16}\text{O } 1_{11} - 0_{00}$ transition we conclude that the $S \cdot \eta_B$ is 0.38 K for H_2^{16}O . Therefore only a fraction ($f=17\%$) of the total dust continuum is covered by the

blue lobe of the outflow. This fraction is calculated from

$$f = 1 - \frac{T_{MB} - S \cdot \eta_B}{T_c},$$

where T_{MB} is the detected signal strength and T_c is the level of the background continuum. No emission is seen from the red lobe of the $1_{11} - 0_{00}$ line of the rarer isotopologues, and therefore only an upper limit of 0.1 K can be given for the corresponding $S \cdot \eta_B$. Because this upper limit is of the order of the measurement uncertainty of the signal of both lines, we calculated the optical depth and column density of the $\text{H}_2^{17}\text{O } 1_{11} - 0_{00}$ and $\text{H}_2^{18}\text{O } 1_{11} - 0_{00}$ lines assuming a source function of zero (all molecules are in the ortho- or para-ground state). This agrees with the physical parameters found in previous investigations (e.g., $T_K > 15$ K, $n(\text{H}_2) > 10^3 \text{ cm}^{-3}$; Leurini et al. 2006). We calculated the optical depth for each velocity channel with the formula

$$\tau = -\ln\left(\frac{T_{MB} - (1 - f) \cdot T_c}{f \cdot T_c}\right),$$

and the corresponding column density as described in Sect. 3.1. The maximum optical depths ($v_{\text{lsr}} = -25.7 \text{ km s}^{-1}$) are 0.70 and 0.29 for H_2^{18}O and $\text{H}_2^{17}\text{O } 1_{11} - 0_{00}$, respectively. The corresponding column densities are $4.1 \pm 0.6 \cdot 10^{13} \text{ cm}^{-2}$ and $1.1 \pm 0.3 \cdot 10^{13} \text{ cm}^{-2}$ for p- H_2^{18}O and p- H_2^{17}O . Hence the resulting $\text{H}_2^{18}\text{O}/\text{H}_2^{17}\text{O}$ ratio is 3.7 ± 0.6 , which agrees well with the values of the $^{18}\text{O}/^{17}\text{O}$ ratio reported in the literature (e.g., Wilson & Rood 1994). Assuming the same continuum coverage for the $\text{H}_2^{17}\text{O } 1_{10} - 1_{01}$ line, we calculated the o- H_2^{17}O column density in a similar way, which leads to an optical depth of 0.34, which in turn resulted in a column density of $2.7 \pm 1 \cdot 10^{13} \text{ cm}^{-2}$. Thus the o/p ratio in the outflow is 2.5 ± 0.8 . The higher o/p ratio in the outflow is consistent with the gas being warmer (> 50 K) compared to the foreground clouds. Comparing these values to the total column density of the outflow determined by Leurini et al. (2006), and assuming an $\text{H}_2^{16}\text{O}/\text{H}_2^{18}\text{O}$ ratio of 500, we derive a water abundance of $4.3 \cdot 10^{-5}$, a value typical for warm (> 100 K) gas.

4. Summary

Herschel/HIFI studies of multiple lines of water isotopologues give important insights into the physical processes in dense molecular material. Our observations of NGC 6334 I indicate that

- H_2O lines show complex line profiles, with multiple emission and absorption features, originating from multiple spatial components.
- the H_2O abundance varies between about $4 \cdot 10^{-5}$ in the outflow, $2 \cdot 10^{-6}$ in the hot core, and 10^{-8} in the cool foreground gas. These abundances are in the range of previously determined ISM values.
- the $\text{H}_2^{18}\text{O}/\text{H}_2^{16}\text{O}$ and $\text{H}_2^{17}\text{O}/\text{H}_2^{16}\text{O}$ ratios are comparable to the $^{18}\text{O}/^{16}\text{O}$ and $^{17}\text{O}/^{16}\text{O}$ isotopic ratios determined from observations of the CO isotopologues.
- the water o/p ratio appears to be lower than the statistical value of three in the cold, quiescent material, whereas it is close to three in the warmer outflow gas. The lower o/p ratio in the foreground component may be explained by proton exchange reactions with H^+ and H_3^+ , which lower the o/p ratio to a value corresponding to the gas kinetic temperature of about 20 K.

Observations of many additional water lines will be available in the future, when the complete spectral scan of NGC 6334 I is carried out. This will allow a more detailed modeling of water abundances in this interesting source.

References

- Beuther, H., Walsh, A. J., Thorwirth, S., et al. 2008, *A&A*, 481, 169
 Beuther, H., Walsh, A. J., Thorwirth, S., et al. 2007, *A&A*, 466, 989
 Bjerkeli, P., Liseau, R., Olberg, M., et al. 2009, *A&A*, 507, 1455
 Boonman, A. M. S., Doty, S. D., van Dishoeck, E. F., et al. 2003, *A&A*, 406, 937
 Comito, C., & Schilke, P. 2002, *A&A*, 395, 357
 Ellingsen, S. P., von Bibra, M. L., McCulloch, P. M., et al. 1996, *MNRAS*, 280, e78
 de Graauw, Th., et al. 2010, *A&A*, in press
 de Pree, C. G., Rodriguez, L. F., Dickel, H. R. & Goss, W. M. 1995, *ApJ*, 447, 220
 Hogerheijde, M. R. & van der Tak, F. F. S. 2000, *A&A*, 362, 697H
 Hunter, T. R., Brogan, C. L., Megeath, S. T., et al. 2006, *ApJ*, 649, 888
 Kraemer, K. E. & Jackson, J. M. 1995, *ApJ*, 439, 9
 Leurini, S., Schilke, P., Parise, B., et al. 2006, *A&A*, 454, 83
 Lis, D. C., Phillips, T. G., Goldsmith, P. F., et al. 2010, in press (this issue)
 Maercker, M., Schier, F. L., Olofsson, H., et al. 2008, *A&A* 479, 779791
 Matthews, H. E., McCutcheon, W. H., Kirk, H., et al. 2008, *AJ*, 136, 2083
 Melnick, G. J. & Bergin, E. A. 2005, *AdSpR*, 36, 1027
 Mumma, M. J., Weaver, H. A. & Larson, H. P. 1987, *A&A*, 187, 419
 Neckel, T. 1978, *A&A*, 69, 51
 Neufeld, D. A. & Melnick, G. J. 1991, *ApJ*, 368, 215
 Ott, S., 2010, in ASP Conference Series, *Astronomical Data Analysis Software and Systems XIX*, Y. Mizumoto, K.-I. Morita, and M. Ohishi, eds., in press
 Pilbratt, G., et al. 2010, *A&A*, in press
 Sandell, G. 2000, *A&A*, 358, 242
 Schilke, P., Comito, C., Thorwirth, S., et al. 2006, *A&A*, 454, 41
 Straw, S. M. & Hyland, A. R. 1989, *ApJ*, 340, 318
 Stutzki, J. & Winnewisser, G. 1985, *A&A*, 144, 13
 Thorwirth, S., Winnewisser, G., Megeath, S. T. & Tieftrunk, A. R. 2003, *ASPC*, 287, 257
 van der Tak, F. F. S., et al. 2010, *A&A*, in press (Herschel Special Issue)
 van der Wiel, M. H. D., van der Tak, F. F. S., Lis, D. C., et al. 2010, *A&A*, in press (this Issue)
 van Dishoeck, E. F. & Helmich, F. P. 1996, *A&A*, 315, 177
 Walsh, A. J., Longmore, S. N., Thorwirth, S., et al. 2007, *MNRAS*, 382, 35
 Wilson, T. L. & Rood, R. 1994, *ARA&A*, 32, 191
 Zmuidzinas, J., Blake, G. A., Carlstrom, J., et al. 1995, *ApJ*, 447, 125

Acknowledgements. HIFI has been designed and built by a consortium of institutes and university departments from across Europe, Canada and the United States under the leadership of SRON Netherlands Institute for Space Research, Groningen, The Netherlands and with major contributions from Germany, France and the US. Consortium members are: Canada: CSA, U. Waterloo; France: CESR, LAB, LERMA, IRAM; Germany: KOSMA, MPIfR, MPS; Ireland, NUI Maynooth; Italy: ASI, IFSI-INAF, Osservatorio Astrofisico di Arcetri-INAF; Netherlands: SRON, TUD; Poland: CAMK, CBK; Spain: Observatorio Astronómico Nacional (IGN), Centro de Astrobiología (CSIC-INTA). Sweden: Chalmers University of Technology - MC2, RSS & GARD; Onsala Space Observatory; Swedish National Space Board, Stockholm University - Stockholm Observatory; Switzerland: ETH Zurich, FHNW; USA: Caltech, JPL, NHSC. We thank many funding agencies for financial support.

- ¹ California Institute of Technology, Pasadena, USA
² Université de Bordeaux, Laboratoire d'Astrophysique de Bordeaux, France; CNRS/INSU, UMR 5804, Floirac, France
³ Laboratoire d'Astrophysique de Grenoble, UMR 5571-CNRS, Université Joseph Fourier, Grenoble France
⁴ INAF - Istituto di Fisica dello Spazio Interplanetario, Roma, Italy
⁵ Infrared Processing and Analysis Center, Caltech, Pasadena, USA
⁶ CESR, Université Toulouse 3 and CNRS, Toulouse, France

- ⁷ School of Physics and Astronomy, University of Leeds, Leeds UK
⁸ Observatoire de Paris-Meudon, LERMA UMR CNRS 8112, Meudon, France
⁹ Centro de Astrobiología, CSIC-INTA, Madrid, Spain
¹⁰ Max-Planck-Institut für Radioastronomie, Bonn, Germany
¹¹ INAF Osservatorio Astrofisico di Arcetri, Florence Italy
¹² Astronomical Institute 'Anton Pannekoek', University of Amsterdam, Amsterdam, The Netherlands
¹³ Department of Astrophysics/IMAPP, Radboud University Nijmegen, Nijmegen, The Netherlands
¹⁴ IGN Observatorio Astronómico Nacional, Alcalá de Henares, Spain
¹⁵ Jet Propulsion Laboratory, Caltech, Pasadena, CA 91109, USA
¹⁶ SRON, Groningen, The Netherlands
¹⁷ Ohio State University, Columbus, OH, USA
¹⁸ Center for Astrophysics, Cambridge MA, USA
¹⁹ Johns Hopkins University, Baltimore MD, USA
²⁰ Physikalisches Institut, Universität zu Köln, Köln, Germany
²¹ Institut de RadioAstronomie Millimétrique, Grenoble - France
²² Leiden Observatory, Leiden University, Leiden, The Netherlands
²³ Department of Physics and Astronomy, University College London, London, UK
²⁴ INAF - Osservatorio Astronomico di Roma, Monte Porzio Catone, Italy
²⁵ Department of Astronomy, University of Michigan, Ann Arbor, USA
²⁶ Max-Planck-Institut für Astronomie, Heidelberg, Germany
²⁷ Max-Planck-Institut für Sonnenphysikforschung, Lindau, Germany

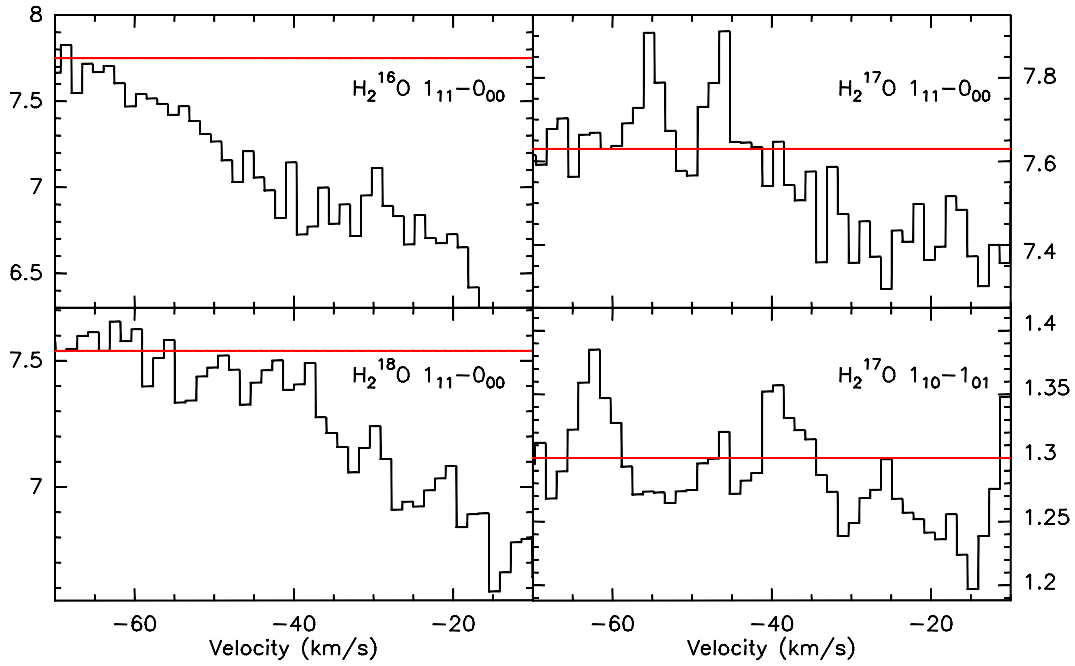


Fig. 2. Absorption feature of the blue lobe of the outflow. The spectra of the ground-state transitions of p-H₂¹⁶O, p-H₂¹⁸O, p-H₂¹⁷O, and o-H₂¹⁷O are displayed. The red line shows the dust continuum level.

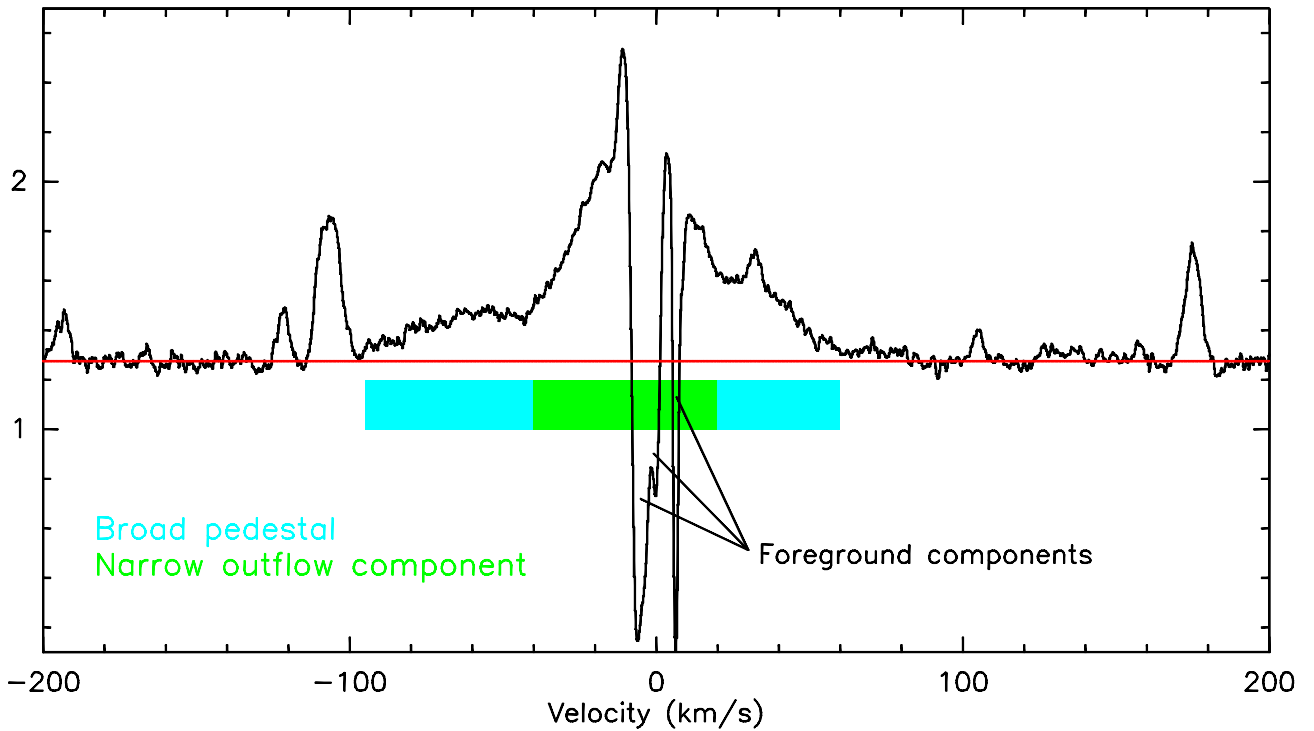


Fig. 3. Spectrum of H₂¹⁶O 1₁₀-1₀₁. The red line marks the dust continuum level. The foreground components and the two outflow components are labeled. The velocity range of the broad outflow (pedestal) is marked in light blue and the range of the narrow outflow component is marked in yellow.

Table 2. Summary of the observed lines

Transition	spin	E_{low} [K]	ν [GHz]	beam size [$''$]
$\text{H}_2^{16}\text{O } 6_{24} - 7_{17}$	p	844.2	488.491	44
$\text{H}_2^{18}\text{O } 1_{10} - 1_{01}$	o	34.3	547.676	41
$\text{H}_2^{17}\text{O } 1_{10} - 1_{01}$	o	34.3	552.021	41
$\text{H}_2^{16}\text{O } 1_{10} - 1_{01}$	o	34.3	556.936	41
$\text{H}_2^{16}\text{O } 5_{32} - 4_{41}$	o	702.0	620.701	33
$\text{H}_2^{18}\text{O } 2_{11} - 2_{02}$	p	100.7	745.320	30
$\text{H}_2^{16}\text{O } 2_{11} - 2_{02}$	p	100.9	752.033	30
$\text{H}_2^{16}\text{O } 4_{22} - 3_{31}$	p	410.6	916.172	25
$\text{H}_2^{16}\text{O } 3_{12} - 3_{03}$	o	196.9	1097.365	20
$\text{H}_2^{18}\text{O } 1_{11} - 0_{00}$	p	0.0	1101.698	20
$\text{H}_2^{17}\text{O } 1_{11} - 0_{00}$	p	0.0	1107.167	20
$\text{H}_2^{16}\text{O } 1_{11} - 0_{00}$	p	0.0	1113.343	20

Table 3. Parameters of the narrow absorption features seen in the two ground-state H_2^{16}O transitions. $\int T_{MB} dv$ is the intensity integrated over the velocity ranges of the individual components (Table 1). The continuum level given is an average value for the individual components.

Line	v_{lsr} km/s	T_{MB} K	$\int T_{MB} dv$ K km s $^{-1}$	cont. level K
	-6.2 \pm 0.3	0.21 \pm 0.17	6.2 \pm 0.31	7.7 \pm 0.4
$1_{11}-0_{00}$	-0.34 \pm 0.1	1.87 \pm 0.17	7.8 \pm 0.39	7.7 \pm 0.4
	+6.1 \pm 0.10	0.33 \pm 0.17	7.8 \pm 0.39	9.0 \pm 0.45
	-6.8 \pm 1.0	0.22 \pm 0.024	2.04 \pm 0.10	1.54 \pm 0.08
$1_{10}-1_{01}$	-0.25 \pm 0.1	0.81 \pm 0.024	2.69 \pm 0.13	1.53 \pm 0.08
	+6.3 \pm 0.10	0.19 \pm 0.024	2.36 \pm 0.76	1.51 \pm 0.08

Table 4. Hot core line parameters

Line	$\int T_{MB} dv$ K kms $^{-1}$	v_{lsr} kms $^{-1}$	Δv kms $^{-1}$	T_{MB} K
$\text{H}_2^{16}\text{O } 4_{22}-3_{31}$	4.96 \pm 0.11	-8.3 \pm 0.11	6.1 \pm 0.27	0.66 \pm 0.04
$\text{H}_2^{16}\text{O } 6_{24}-7_{17}$	0.28 \pm 0.04	-8.1 \pm 0.16	3.8 \pm 0.41	0.084 \pm 0.012
$\text{H}_2^{16}\text{O } 5_{32}-4_{41}$	4.80 \pm 0.06	-8.6 \pm 0.60	7.8 \pm 0.14	0.522 \pm 0.013
$\text{H}_2^{18}\text{O } 2_{11} - 2_{02}$	3.2 \pm 0.2	-8.6 \pm 0.3	6.3 \pm 0.5	0.46 \pm 0.05